IOP Publishing and International Atomic Energy Agency Nuclear Fusion

Nucl. Fusion **49** (2009) 104008 (15pp) doi:10.1088/0029-5515/49/10/104008

DIII-D research in support of ITER

E.J. Strait[a] **for the DIII-D Team**

General Atomics, San Diego, CA, USA

E-mail: strait@fusion.gat.com

Received 31 March 2009, accepted for publication 12 June 2009
Published 9 September 2009
Online at stacks.iop.org/NF/49/104008

Abstract

DIII-D research is providing key information for the design and operation of ITER. Investigations of axisymmetric stability and of edge-localized mode (ELM) suppression with resonant magnetic perturbations have helped provide the physics basis for new axisymmetric and non-axisymmetric control coils in ITER. Discharges that simulate ITER operating scenarios in conventional H-mode, advanced inductive, hybrid and steady state regimes have achieved normalized performance consistent with ITER's goals for fusion performance. Stationary discharges with high β_N and 90% non-inductive current that project to $Q = 5$ in ITER have been sustained for a current relaxation time ($\sim$2.5 s), and high beta wall-stabilized discharges with fully non-inductive current drive have been sustained for more than one second. Detailed issues of plasma control have been addressed, including the development of a new large-bore startup scenario for ITER. DIII-D research also contributes to the basis for reliable operation in ITER, through active control of the chief performance-limiting instabilities. Simultaneous stabilization of neoclassical tearing modes (by localized current drive) and resistive wall modes (by magnetic feedback) has allowed stable operation at high beta and low rotation. In research aimed at improving the lifetime of material surfaces near the plasma, recent experiments have investigated several approaches to mitigation of disruptions, including injection of low-Z gas and low-Z pellets, and have shown the conditions that minimize core impurity accumulation during radiative divertor operation. Investigation of carbon erosion, transport and co-deposition with hydrogenic species, and methods for the removal of co-deposits, will contribute to the physics basis for initial operation of ITER with a carbon divertor. A broad research programme provides the physics basis for predicting the performance of ITER. Recent key results include the discovery that the L–H power threshold is reduced with low neutral beam torque, and the development of a successful model for prediction of the H-mode pedestal height in DIII-D. Research areas with the potential to improve ITER's performance include the demonstration of ELM-free 'quiescent H-mode' discharges with both co- and counter-neutral beam injection, and validation of the predicted torque generated by static, non-axisymmetric magnetic fields. New diagnostics provide detailed benchmarking of turbulent transport codes and direct measurements of the anomalous transport of fast ions by Alfvén instabilities. Successful comparison of experiment and modelling for off-axis neutral beam current drive provides the basis for more flexible current profile control in advanced scenarios.

PACS numbers: 52.55.Fa, 52.25.Fi, 52.55.Pi, 52.55.Rk, 52.55.Tn, 52.55.Wq

(Some figures in this article are in colour only in the electronic version)

1. Introduction

DIII-D research is aimed at providing the physics basis to optimize the tokamak approach to fusion energy production, and much of the programme directly supports the design and future operation of ITER. Recent DIII-D research has addressed specific, near-term issues for ITER such as design of new coils for suppression of edge-localized modes (ELMs) and specification of poloidal field systems for control of plasma shape and vertical stability. A longer term goal is to develop and characterize ITER-relevant operating scenarios that integrate high fusion performance, stable operation and appropriate boundary conditions, ultimately simulating the entire discharge evolution (breakdown, ramp-up, flattop and ramp-down). Recent experiments include discharges that demonstrate normalized performance consistent with ITER's $Q = 10$ mission, and significant progress has been made towards scenarios with 100% non-inductive current for the $Q = 5$ steady-state goal. DIII-D also contributes to a broad scientific base for tokamak physics that will help to optimize fusion performance in ITER.

As summarized in this paper, DIII-D research has provided guidance on the physics requirements for ELM control with resonant magnetic perturbations (RMPs), and for axisymmetric stability control in ITER (section 2). DIII-D

[a] Author to whom any correspondence should be addressed.

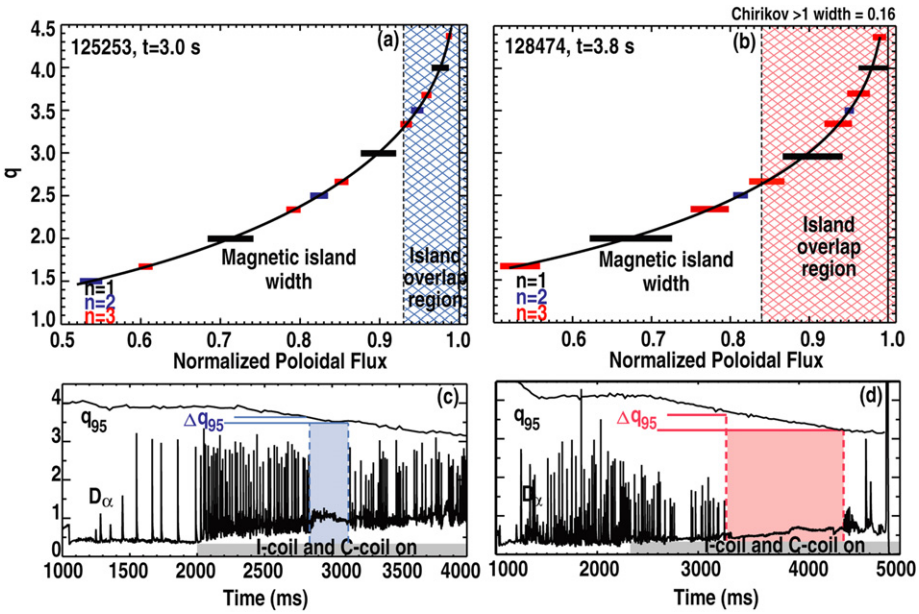

Figure 1. Two discharges with ELM suppression by RMPs, showing (*a*), (*b*) q-profile with calculated magnetic island widths and (*c*), (*d*) time evolution of q_{95} and divertor D_α emission. Changing the non-axisymmetric coil currents in the second case creates a larger region of island overlap (*b*), and ELM suppression is observed over a larger window in safety factor, Δq_{95} (*d*). In terms of normalized poloidal flux, the width of the edge region with Chirikov parameter greater than unity is (*a*) $\Delta\Psi_N = 0.07$ and (*b*) $\Delta\Psi_N = 0.16$.

experiments that simulate several specific high-gain and steady-state scenarios envisioned for ITER provide a platform for projections of fusion performance and tests of plasma control (section 3). Progress towards the understanding and active control of magnetohydrodynamic (MHD) instabilities is contributing to the basis for stable and reliable operation in ITER, while the development of disruption mitigation and means to control the plasma-wall interface will help to improve the lifetime of plasma-facing components (section 4). Finally, investigations of the physics of plasma rotation, transport, stability and wave-particle interactions contribute to the basis for prediction and improvement of ITER's performance (section 5). Future DIII-D research will continue to investigate these issues and to provide the basis for high-performance steady-state operation of ITER.

2. ITER baseline design

DIII-D research has contributed to the recent evaluation of the ITER physics requirements [1]. Key areas include the control of ELMs and of axisymmetric stability. The assessment of results from DIII-D and other existing tokamaks has led to guidelines for proposed new coil systems in ITER for the purposes of ELM suppression [2] and vertical position control [3].

2.1. Edge-localized modes

The suppression of ELM instabilities by RMPs offers a promising method to reduce the erosion of ITER's divertor targets. Recent analysis has shown that the impulsive energy loss due to ELMs must be reduced by a factor of ∼20 or eliminated entirely in order to maintain an acceptable lifetime for the divertor targets [4]. DIII-D experiments with RMPs

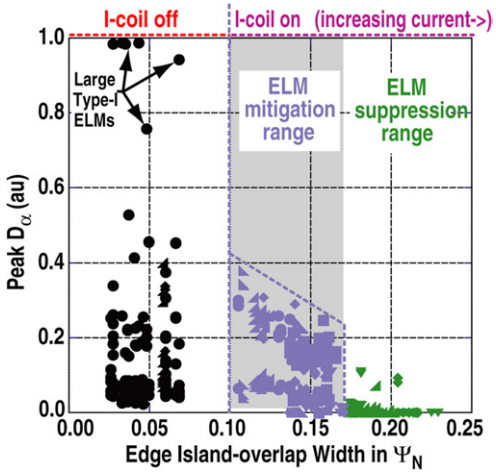

Figure 2. ELM size (peak D_α emission) versus width $\Delta\Psi_N$ (in normalized poloidal flux) of the edge island overlap region, for a set of discharges with ITER-like shape and collisionality.

applied by non-axisymmetric coils internal to the vacuum vessel have demonstrated ELM suppression at ITER-like shape and collisionality [5]. ELM suppression occurs only in a resonant window of edge safety factor q_{95}, as seen in figures 1(*a*) and (*c*). However, the operating range in q_{95} can be increased by varying the coil current and magnetic spectrum in such a way as to increase the degree of island overlap and the width of the resulting stochastic layer at the plasma edge (figures 1(*b*) and (*d*)). The ELM behaviour is correlated with the width of the edge region where the Chirikov parameter is calculated to be greater than unity [6]: the ELM size decreases as this width increases, and ELMs are suppressed when the width exceeds about 0.17 in normalized poloidal flux (figure 2). This Chirikov island overlap parameter was used as a guide for

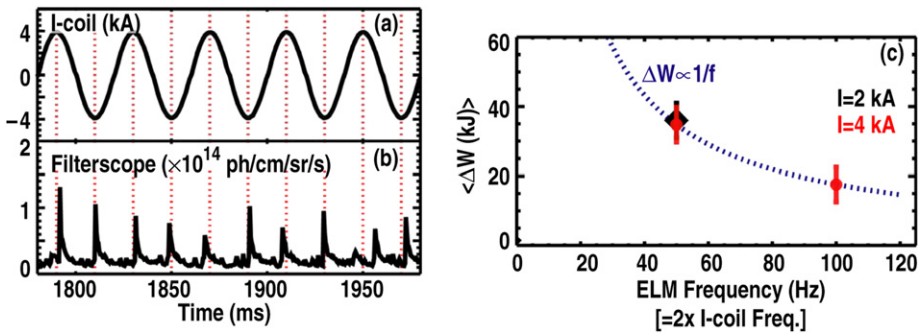

Figure 3. Effect on ELMs of a non-resonant, oscillating $n = 3$ magnetic perturbation, showing the time evolution of (a) perturbation coil current and (b) divertor D_α emission and (c) the energy loss per ELM as a function of ELM frequency.

assessment of new RMP coil options in ITER. In a comparison of several coil configurations in DIII-D, ELM suppression was obtained with a single row of internal, small aperture, off-midplane coils (at larger current than with two such rows but with about the same RMP field strength), while suppression was not obtained with similar $n = 3$ field amplitude in the pedestal using a single row of external, large aperture, on-midplane coils [7]; these results are consistent with the island overlap criterion, and support the choice of a multi-row, small-aperture coil system for ITER. Pellets injected for core fuelling during ELM suppression are found to generate only small-amplitude bursts of edge recycling, which can be avoided by reducing the RMP amplitude slightly; this result suggests that ELM suppression by RMP is compatible with pellet fuelling. The ELM suppression is a result of enhanced particle transport at the edge; ELITE calculations consistently show discharges with ELM suppression by RMP to be in the stable region of the peeling-ballooning stability diagram [8]. 3D MHD simulation [9] and other work is in progress to determine the physical mechanism responsible for the enhanced particle transport, including a possible role of $E \times B$ convection cells.

Initial experiments have begun to investigate ELM 'pacing' by shallow pellet injection into the pedestal [10], and to investigate a recent, surprising discovery of ELM 'pacing' by modulation of an $n = 3$ magnetic perturbation field. Here the off-midplane coils were configured with a non-resonant poloidal spectrum. When the coils were operated with a sinusoidally oscillating current, the ELM frequency became locked to twice the frequency of the current modulation (figures 3(a) and (b)). The ELM energy loss appears to vary inversely with ELM frequency, as expected (figure 3(c)). The minimum perturbation amplitude required for ELM pacing has not yet been determined.

2.2. Axisymmetric stability

Experiments in DIII-D and other tokamaks have provided guidance [11] for vertical stability requirements in ITER. The metric chosen for these studies was ΔZ_{max}, the largest vertical displacement at which the control system can reverse the vertical motion of the plasma. Experimental measurements of the stability boundary between controllable and uncontrollable displacements (green and red points in figure 4) are in good agreement with model predictions of ΔZ_{max} (solid curve in figure 4), providing validation for modelling of vertical stability control. The DIII-D experiments shown here used

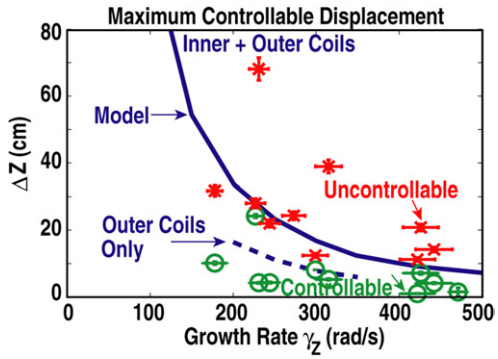

Figure 4. Vertical plasma displacement ΔZ versus uncontrolled growth rate of the axisymmetric instability, with experimental results showing controllable displacements (green points) and uncontrollable displacements (red points), and the corresponding model prediction of the maximum controllable displacement (solid curve). The experimental cases used control with outer and inner poloidal field coils; also shown is the model prediction for control with outer coils only.

coils on both the low field and high field sides of the plasma for vertical control, similar to the VS1 and VS2 circuits in ITER [11]. This configuration approximately doubled the ΔZ_{max} relative to control with low field side coils only (similar to VS1 in ITER). Results from lower single-null discharges in DIII-D and other experiments indicate that $\Delta Z_{max}/a$, the ratio of the maximum controllable vertical displacement to the minor radius, must be at least 5% for safe operation. These results have contributed to the proposed addition of internal vertical stability coils in ITER.

3. Integrated scenario development

A major objective of DIII-D research is the development of ITER-relevant operating scenarios that integrate high fusion performance, stable operation and appropriate boundary conditions. The ultimate goal is demonstration of a complete scenario including ramp-up, sustained performance in stationary 'flattop' conditions and rampdown.

3.1. ITER demonstration scenarios

This year, we have focused on evaluation of flattop performance in four operating scenarios for ITER, using

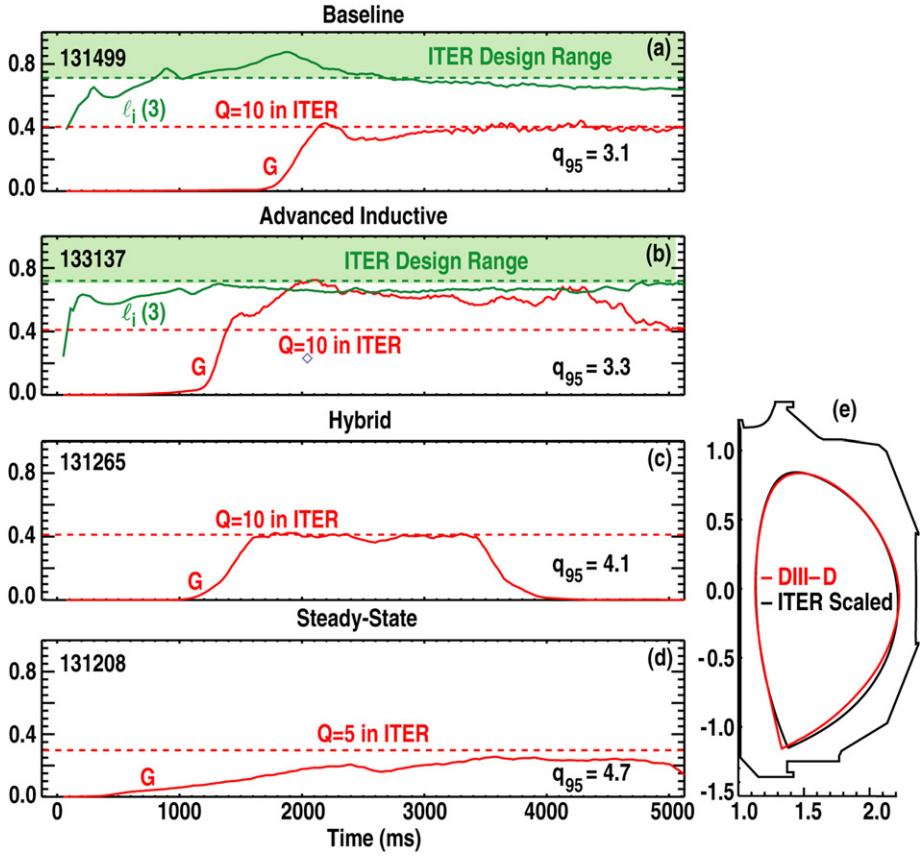

Figure 5. ITER demonstration discharges characterized by fusion figure of merit $G = \beta_N H_{89}/q_{95}^2$ and internal inductance $l_i(3)$, for cases including (*a*) baseline scenario with $q_{95} \sim 3$ and $\beta_N \sim 2$ (ITER equivalent $I_p = 15$ MA), (*b*) advanced inductive scenario with $q_{95} \sim 3.3$ and $\beta_N \sim 2.8$ (ITER equivalent $I_p = 15$ MA), (*c*) hybrid scenario with $q_{95} \sim 4.1$ and $\beta_N \sim 2.8$ (ITER equivalent $I_p = 12$ MA) and (*d*) steady-state scenario with $q_{95} \sim 4.7$ and $\beta_N \sim 2.8$–3.0 (ITER equivalent $I_p = 9$ MA). Also shown is (*e*) the DIII-D discharge shape compared with the scaled-down ITER shape.

DIII-D discharges with the ITER aspect ratio and cross-section (figure 5) but scaled down in size [12]. These discharges allow a direct comparison, in a single device, of the fusion performance and operating characteristics of these scenarios. To date, the emphasis has been on reproducing global parameters such as discharge shape, aspect ratio, safety factor and normalized beta; future work will begin to address other dimensionless parameters such as collisionality and T_i/T_e. As summarized in figure 5, the cases studied include the conventional H-mode baseline scenario (ITER scenario 2), an advanced inductive scenario (aimed at the goal of $Q = 30$ in ITER), the 'hybrid' scenario (ITER scenario 3) and the steady-state scenario (ITER scenario 4). In all four cases, the fusion performance characterized by $G = \beta_N H_{89}/q_{95}^2$ reaches or exceeds the level required for ITER's goals: fusion gain $Q \geqslant 10$ for the first three cases and $Q = 5$ for the steady-state case. (Here $\beta_N = \beta(aB/I)$ is the normalized beta and H_{89} is energy confinement time normalized to the ITER89P L-mode scaling [13].) Recently, fusion performance consistent with $Q > 10$ in ITER has also been demonstrated in advanced inductive discharges with low neutral beam torque, and hybrid mode operation has been shown to be compatible with ELM suppression [14]. High beta wall-stabilized scenarios compatible with steady-state operation have been sustained with a stationary current density profile for 2.5 s, or about one current relaxation time.

The small differences from the ITER shape seen in figure 5(*e*) are motivation for a study of the sensitivity of fusion performance to discharge shape; initial results indicate that the triangularity can influence performance through the stability of the H-mode pedestal. These discharges also displayed several issues known to be of concern for ITER, including large infrequent ELMs, and neoclassical tearing modes (NTMs) that lead to confinement degradation or disruption. These contribute to the motivation for the study of ELM suppression coils (section 2) andNTM stabilization (section 4). As seen in figures 5(*a*) and (*b*), the internal inductance in the DIII-D baseline and advanced inductive discharges was found to lie at or below the lower limit of the ITER specification [$0.7 < l_i(3) < 1.0$], potentially leading to a loss of shape control capability. (See [15] for a definition of $l_i(3)$.) This result has motivated recommendations for an increase in poloidal field coil current capabilities and a change in the divertor coil location.

3.2. *Plasma startup*

DIII-D discharges have also been used to study the detailed evolution and control of ITER startup scenarios [15]. In these experiments, the discharge shape and aspect ratio were matched to those anticipated for ITER, and the time evolution was scaled from that of the planned ITER scenario by the

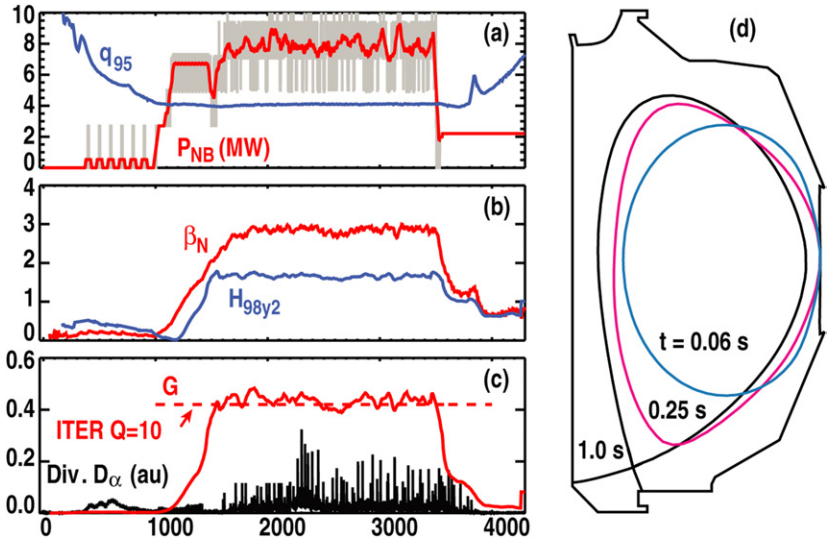

Figure 6. ITER demonstration discharge with large-bore startup, showing (*a*) neutral beam power P_{NB} and safety factor q_{95}; (*b*) normalized beta β_N and normalized energy confinement H_{98y2}; (*c*) divertor D_α emission and fusion figure of merit $G = \beta_N H_{89}/q_{95}^2$ and (*d*) discharge cross section. The discharge becomes diverted at $t = 0.27$ s.

ratio of the plasma L/R times. The 'small-bore' scenario initially envisioned for startup of ITER plasmas was shown in DIII-D experiments to result in values of $l_i(3)$ up to 1.2, significantly larger than the ITER specification of $0.7 < l_i(3) < 1.0$, with the potential for difficulties with vertical stability control. A new 'large-bore' startup was demonstrated on DIII-D (figure 6), in which the plasma is initiated on the outer limiter with a large cross-section, and goes to an x-point configuration early in the current ramp. This scenario reduces the heat load on the limiter and reduces the internal inductance. The example shown in figure 6 leads to a hybrid scenario with fusion performance factor $G = 0.4$, sufficient for the goal of $Q = 10$ in ITER.

The example shown in figure 6 used no auxiliary heating (other than short neutral beam pulses for diagnostic measurements) until near the end of the plasma current ramp. However, other experiments have studied the use of electron cyclotron heating (ECH) assisted breakdown and startup [15]. With the use of ECH at plasma initiation, the large-bore startup has proved robust with toroidal electric fields as low as 0.21 V m^{-1} (the ITER specification is 0.3 V m^{-1}) and smaller resistive flux consumption. Feedback control of internal inductance during the current ramp has been developed, using dI_p/dt as the actuator; this helps to avoid stability limits and to improve the control over the plasma configuration in the flattop phase.

3.3. Steady-state scenarios

Two approaches are being pursued at DIII-D towards steady-state, non-inductive discharges [16] for ITER and devices beyond ITER. The first approach is a high q_{min}, wall-stabilized configuration at moderate β_N, similar to ITER's scenario 4. High triangularity double-null plasmas were used, and the plasma squareness was optimized with respect to stability limits and confinement (figures 7 (*a*) and (*b*)), allowing higher beta and higher bootstrap fraction. Closed loop feedback control of the evolution of q_{min} during the plasma current ramp-up and early flattop, using ECH to modify T_e, sets the value of q_{min} at the start of the high β_N phase. With over 3 MW of electron cyclotron current drive (ECCD) applied broadly at $q \lesssim 2$, NTMs were avoided (through current profile modification rather than direct stabilization) and discharges with $\beta_N \sim 3.5$, bootstrap current fractions of 60–70%, and fully non-inductive current sustainment for more than one second were obtained (figure 7(*c*)). In these discharges the duration was limited only by the available pulse length of the heating and current drive sources.

The second approach aims to achieve high β_N without the need for wall stabilization, by operation at higher $l_i \sim 1.1$, again in a high triangularity double-null configuration. In this case, the central safety factor is near unity and the associated strong magnetic shear contributes to higher stability limits and energy confinement. Such discharges have reached $\beta_N = 5$ transiently, with non-inductive current fraction greater than unity (up to 90% bootstrap current) and very good energy confinement (figure 8). The loop voltage (not shown) is slightly negative, which is consistent with the calculated non-inductive fraction exceeding unity. In this example, the normalized beta is well above 4, but remains near the ideal MHD no-wall kink stability limit and below the ballooning stability limit (figure 8(*a*)). Active MHD spectroscopy—measurement of the stable kink mode's damping rate by exciting it at low amplitude with external coils—shows a reduction in the stability of the $n = 1$ kink mode at peak beta, consistent with the stability calculations showing that beta may slightly exceed the ideal MHD no-wall kink stability limits at $\beta_N > 4$. However, these results suggest that a similar scenario might provide access to $\beta_N > 3$ in ITER without the need for wall stabilization.

4. Control solutions for ITER

Progress in DIII-D towards the understanding and control of MHD instabilities is contributing to the basis for stable and reliable operation in ITER. Work here includes investigation of the effects of rotation and error fields in plasma stability,

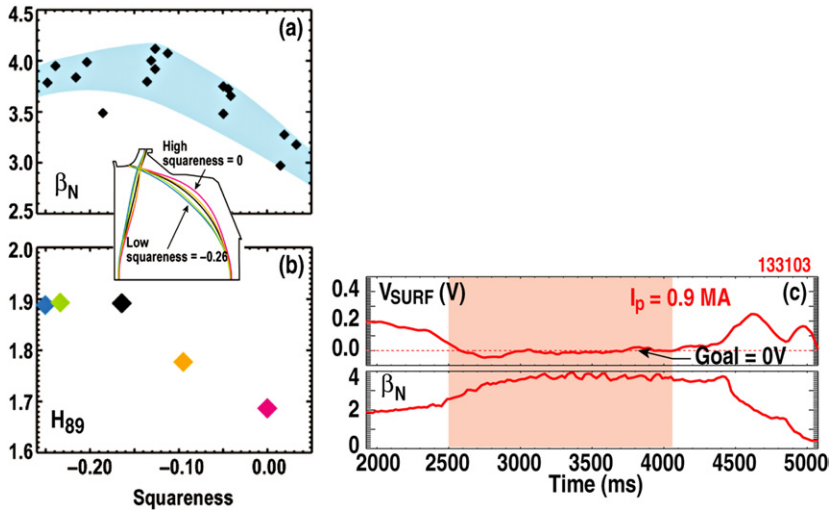

Figure 7. Candidate steady-state scenario, with $q_{min} \geqslant 1.5$ and $q_{95} \sim 6$, showing optimization of discharge squareness with respect to (*a*) normalized beta β_N and (*b*) normalized energy confinement H_{89} and (*c*) time evolution of surface loop voltage V_{SURF} and normalized beta β_N.

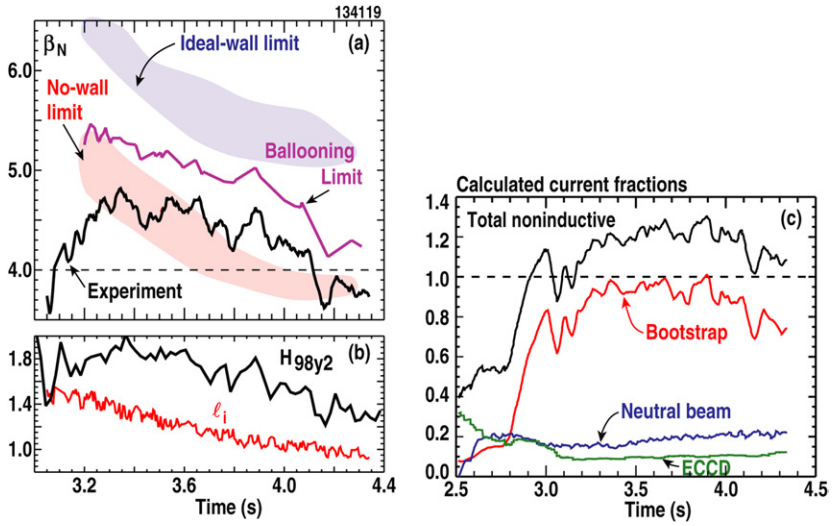

Figure 8. High beta discharge at higher internal inductance, with $q_{min} \gtrsim 1$ and $q_{95} \sim 7$–8, showing (*a*) normalized beta β_N with calculated ballooning and $n = 1$ kink stability limits; (*b*) normalized energy confinement H_{98y2} and internal inductance l_i and (*c*) calculated non-inductive current fraction with contributions from bootstrap, neutral beam and electron cyclotron driven currents.

stabilization of NTMs with modulated ECCD and stabilization of resistive wall modes (RWMs) with direct feedback control. DIII-D research is also aimed at controlling the interaction of the plasma with surrounding materials in order to improve the lifetime of plasma-facing components in fusion devices. Challenges that ITER will face include high transient heat flux and runaway electrons occurring during disruptions, as well as the time-averaged heat flux to the divertor. The proposed use of a carbon divertor during the deuterium phase of operation and possibly early in the D–T phase introduces the additional challenges of understanding the erosion, transport and redeposition of carbon, and of recovering tritium retained in the carbon.

4.1. Error fields

Tokamak plasmas with high beta and low rotation are exceedingly sensitive to error fields. In order to test the role of the ideal kink mode, DIII-D experiments have been carried out in a weakly shaped lower single-null plasma, designed to have a low no-wall stability limit. In these experiments [17] a slowly increasing $n = 1$ magnetic perturbation leads to sudden penetration of the $n = 1$ field, accompanied by collapse of plasma rotation and island formation (figure 9(*a*)). The critical amplitude of the applied perturbation decreases strongly above the no-wall stability limit. However, the resonant response of the marginally stable RWM becomes stronger above the no-wall limit. As a result, the critical amplitude of the plasma response that is observed at the collapse of rotation is independent of beta. This result is consistent with the hypothesis that the braking of rotation is dominated by the plasma response and not simply the externally applied field. The amplitude of the plasma response varies strongly with the poloidal mode spectrum of the applied field, in good agreement with MARS-F [18] calculations; this supports the

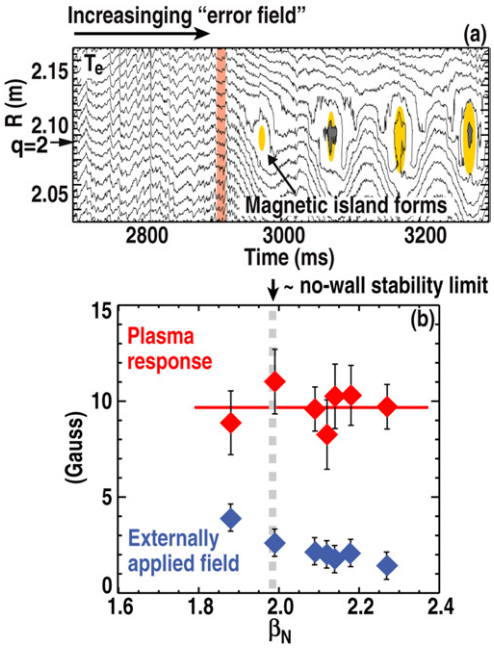

Figure 9. Effect of an applied $n = 1$ 'error field' on a high beta plasma. (a) Electron temperature contours versus time and radius (measured by electron cyclotron emission (ECE)) show island formation above a critical amplitude of the error field. (b) Critical $n = 1$ amplitude as a function of normalized beta β_N, including the critical amplitude of the applied field ($m/n = 2/1$ component, calculated at the $q = 2$ surface) and the critical amplitude of the plasma response (poloidal field, measured at the midplane).

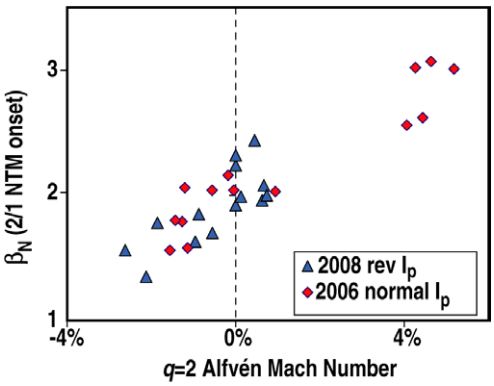

Figure 10. Normalized beta at onset of $m/n = 2/1$ NTM versus rotation velocity (normalized to Alfvén velocity) at the $q = 2$ surface, in an ITER-like single-null plasma.

hypothesis that the plasma response is that of the stable RWM. Experimental evidence also indicates an important role for non-resonant fields, particularly at high plasma rotation. These results indicate that the response of the stable plasma must be considered in projections of error field correction in ITER.

4.2. Neoclassical tearing modes

NTMs are likely to be among the chief performance-limiting instabilities for ITER's baseline scenario. In DIII-D discharges with ITER-like shape, studies with varying neutral beam torque have shown that the beta threshold for onset of 2/1 NTM instabilities decreases as the plasma rotation is reduced to ITER-relevant values (figure 10), consistent with a dependence of the effective Δ' stability parameter on rotational shear [19, 20]. The 2/1 NTM onset also becomes much more sensitive to applied error fields in the low-torque, low-rotation cases. NTM suppression by continuous ECCD has been demonstrated previously; recent DIII-D experiments confirm expectations that the power requirement is reduced by modulation synchronized with the rotating island, using a novel technique to minimize modulation phase errors by detection of the island at the current drive location. DIII-D is contributing to an international effort to understand and model ECCD stabilization of NTMs in ITER [21]. High-quality images of the tearing mode structure using synchronous detection of visible bremsstrahlung emission agree well with an analytic model for the island structure [22], and will allow comparison of island dynamics to more detailed numerical models.

4.3. Resistive wall modes

In DIII-D high beta plasmas at or above the ideal MHD free-boundary stability limit, such as the $Q = 5$ steady-state scenario for ITER, RWMs are stabilized at relatively slow plasma rotation, consistent with theoretical predictions that include kinetic effects [23]. The shaded region in figure 11(a) shows the stable regime and low-rotation threshold, as reported at the 2006 Fusion Energy Conference. These experiments used single-null discharges having a low free-boundary (i.e. no-wall) stability limit. With simultaneous use of ECCD at the $q = 2$ surface to suppress tearing modes, and $n = 1$ magnetic feedback to minimize static error fields and stabilize the plasma response to ELMs and fishbones, recent experiments have achieved stability above the no-wall beta limit at very low rotation [24] (figure 11(b)), below the previously reported threshold. In some cases, stable discharges with low rotation are achieved using only ECCD to suppress NTMs, and without magnetic feedback control of RWMs. This result is consistent with the predicted kinetic stabilization of RWMs at low rotation, and suggests that the observed instabilities are non-rotating NTMs. Nevertheless, in plasmas above the no-wall stability limit, active feedback control plays an important role in suppressing RWMs that are driven by other transient MHD events such as ELMs or fishbones.

4.4. Disruption mitigation

Mitigation of disruptions by rapid injection of various gas species has successfully provided radiative dissipation of the plasma thermal energy and fast plasma current shutdown, reducing thermal loads and vertical forces on the vacuum vessel [25]. However, the $\geqslant 10^{22}$ m^{-3} electron density required for collisional suppression of a runaway electron avalanche (the 'Rosenbluth density') is about an order of magnitude larger than densities achieved to date, and remains a challenge. DIII-D experiments with ITER-like shape and safety factor [26] and 3D nonlinear modelling [27] show that MHD instabilities are important in mixing the impurity gas into the plasma core. DIII-D experiments using a fast rise-time multi-valve system [10] have also shown the importance of delivering the gas to the plasma before the end of the thermal quench; the latter condition favours light gas species, high throughput

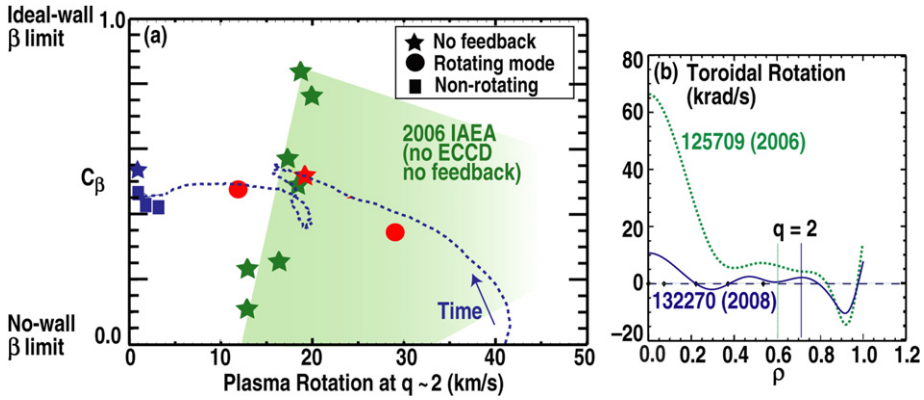

Figure 11. RWM stability at low rotation. (*a*) C_β, the beta value scaled such that $C_\beta = 0$ at the no-wall limit and $C_\beta = 1$ at the ideal-wall limit, versus plasma rotation at the $q = 2$ surface. Squares indicate cases with non-rotating modes, circles indicate cases with rotating modes (most likely NTM) and stars indicate cases without RWM feedback. Included are recent cases with ECCD for suppression of NTMs, and 2006 data without ECCD (green stars). (*b*) Rotation profile at the mode onset in a low-rotation ECCD-stabilized case, compared with a 2006 case without ECCD.

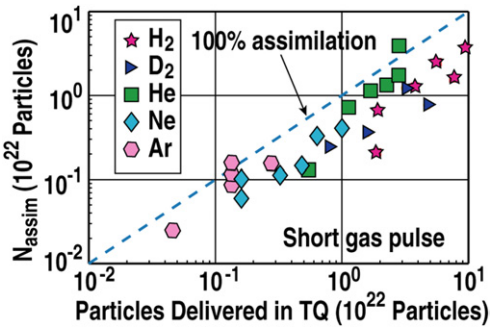

Figure 12. Number of atoms assimilated by the plasma versus number delivered during the thermal quench, for several gas species. The dashed line indicates 100% assimilation.

and delivery systems close to the plasma [28]. Figure 12 shows that the number of atoms assimilated into the plasma increases linearly with the number delivered before the end of the thermal quench, and also shows that more atoms can be delivered quickly with light species owing to the larger thermal speed. A mixture of D_2 + 2% Ne (not shown in figure 12) also appears promising with a large assimilation fraction. Alternative methods for rapid, high-density impurity injection, such as cryogenic pellets [10] and low-Z shell pellets, are being explored.

4.5. Radiative divertor

One way to ameliorate the problem of divertor heating is to introduce 'seed' impurities (e.g. argon) directly into the divertor, where they can radiate a significant fraction of the plasma-conducted power before the plasma particles reach the divertor surface. Leakage of the impurity into the main plasma can be minimized by maintaining a strong flow of deuterium ions into the divertor through upstream deuterium gas puffing and active particle exhaust at the divertor targets. DIII-D experiments show that both the accumulation of argon inside the main plasma and the removal of argon from the divertor are sensitive to the divertor topology and the ion $B \times \nabla B$ drift direction [29, 30]. With argon injection into the private flux region of the upper divertor and the ion $B \times \nabla B$ drift away from the divertor, D_α light shows recycling predominantly at the outer divertor leg (figure 13(*a*)); however, with the ion $B \times \nabla B$ drift towards the divertor, recycling shifts to the inner divertor leg, which often becomes detached and allows argon to leak into the core plasma (figure 13(*c*)). The injected argon also follows the $B \times \nabla B$ drift. The results shown here are for single null discharges, but with a secondary x-point closer than is likely to be the case in ITER; other experiments [30] have compared particle drifts in single null and double-null configurations. Modelling with UEDGE [31], using a new capability to model drifts in a balanced double null configuration, reproduces these key features of the experiments (figures 13(*b*) and (*d*)). The modelling also indicates that the direction of the $E_r \times B$ drift near the x-point may play a key role; in particular, the drift in the private flux region takes ions to the outer divertor in the first case and to the colder inner divertor in the second case. These results show that cross-field drifts may play a key role in predictions of particle exhaust in ITER.

4.6. Carbon walls and tritium retention

Carbon has many advantages as a plasma-facing material, but retention of tritium is a critical issue for its use in ITER, particularly if a carbon divertor is used during the deuterium and early D–T phases of operation. Tritium retention in carbon dust that results from erosion of divertor targets is of concern. DIII-D research is investigating the physics of the transport and co-deposition of carbon and hydrogenic fuel, and methods for removing the co-deposits. Spectroscopic measurements show that the poloidal flow of singly ionized carbon in the scrape-off-layer is decoupled from the core plasma's rotation, but is consistent with an $E_r \times B$ drift due to a radial electric field in the scrape-off-layer [32]. Fast camera imaging now provides information on the quantity and motion of dust particles in DIII-D discharges [33]. Experiments have shown that co-deposition of carbon and deuterium is reduced on heated surfaces [34] and local gas injection has been successful in minimizing co-deposition on diagnostics mirror samples. Laboratory tests of samples taken from DIII-D have shown that thermal oxidation is effective at removing carbon

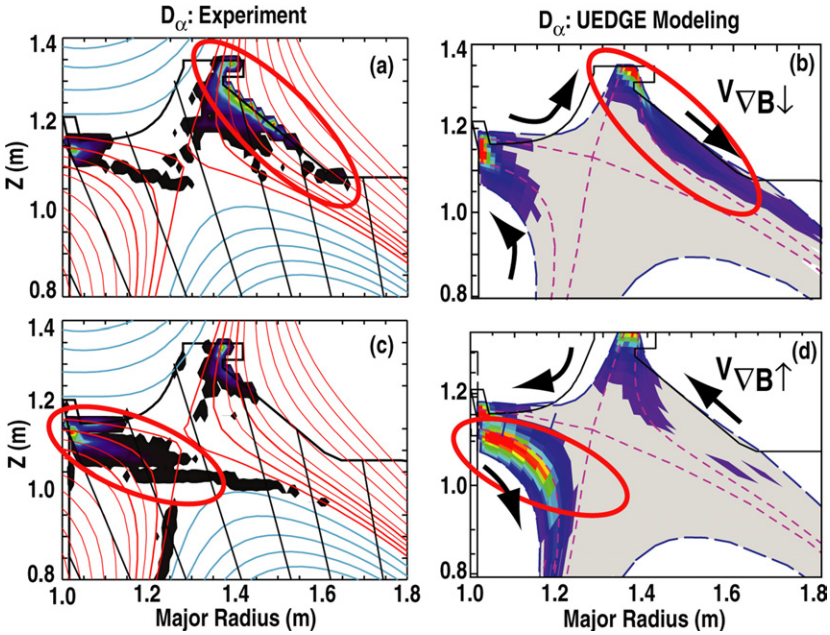

Figure 13. Contours of D_α emission at the upper divertor for cases with the $B \times \nabla B$ drift (a), (b) away from the divertor and (c), (d) towards the divertor. The plots include (a), (c) experimental measurements and (b), (d) UEDGE modelling. Arrows in (b) and (d) show the direction of $E_r \times B$ drift.

co-deposits [35]; tokamak co-deposits have open structures and erode 2–3 orders of magnitude faster than the more dense lab-produced films. Extensive testing has been carried out to determine the effects of oxygen (or air) baking on the various materials found in the DIII-D vacuum vessel, with the ultimate goal of an *in situ* test of co-deposit removal.

5. Physics basis for ITER

Investigations of the physics of transport, stability and wave–particle interactions contribute to the basis for prediction and improvement of ITER's performance. Recent DIII-D results include the improved understanding of plasma rotation in the absence of neutral beam torque, investigation of energy transport and L–H power threshold, improved predictive capability for the H-mode pedestal, progress in understanding and expanding the operating range of the ELM-free quiescent H-mode (QH-mode), detailed benchmarking of gyrokinetic transport calculations against experimental data and progress in measuring and understanding fast-ion transport due to Alfvénic instabilities. The primary emphasis here is on understanding the underlying physics; the experiments summarized in this section use single-null discharges, but other parameters may not be closely matched to those of a specific ITER scenario.

5.1. Plasma rotation

A good understanding of the physics of plasma rotation is important for prediction of ITER's stability and confinement, but the physics of rotation is proving to be complex and subtle [36]. An 'intrinsic' rotation is often seen in tokamak discharges without injected momentum. DIII-D experiments have determined that the anomalous torque associated with

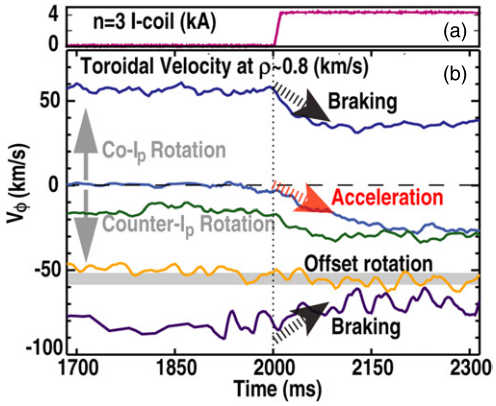

Figure 14. (a) Applied $n = 3$ magnetic perturbation and (b) the resulting evolution of the rotation velocity at $\rho \sim 0.8$ for several discharges with different initial values of rotation.

intrinsic rotation is also present in neutral beam-injected discharges. The anomalous torque is peaked near the edge of the plasma, and is consistent with a model of thermal ion orbit loss [37]. In addition, neoclassical theory predicts that non-RMPs can create a torque of the form $T_{\mathrm{NRMF}} \sim (V_\phi - V_\phi^0)$—that is, a friction-like torque that drives the rotation velocity not towards zero, but towards an 'offset' velocity V_ϕ^0 with a magnitude on the order of the ion diamagnetic drift but in the electron diamagnetic drift direction. This effect has been observed in high beta DIII-D plasmas [38]. As seen in figure 14, the application of a static, non-resonant $n = 3$ magnetic perturbation causes the rotation to approach an offset value of about $-50\,\mathrm{km\,s^{-1}}$; in cases where the initial velocity is near zero or slightly negative, this represents an *increase* in speed when the perturbation is applied. Such torques from

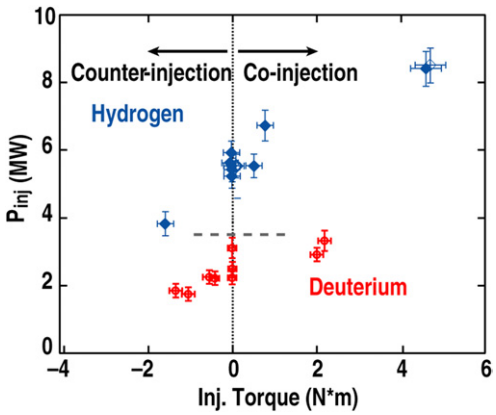

Figure 15. Comparison of L–H threshold power versus neutral beam torque in hydrogen and deuterium plasmas with matching shape (SN), plasma current, toroidal field and density.

non-axisymmetric fields may play an important role in ITER, where the neutral beam torque will be small.

5.2. L–H mode power threshold

Understanding of the L–H power threshold and H-mode energy confinement, and their dependence on ion mass, is of key importance to ITER since the initial phase of ITER operation is planned to be with hydrogen and/or helium plasmas. Previous DIII-D experiments in deuterium plasmas have shown that the L–H power threshold is reduced at low or negative torque [39], and more recently a similar result was obtained in hydrogen [40]. This is a potentially favourable result for ITER, since previous L–H threshold scalings have been based on discharges with strong co-injection. In these experiments, hydrogen was used for both fuelling and neutral beam heating, yielding a measured hydrogen purity (relative to the residual deuterium) of more than 90%. The L–H power threshold in hydrogen plasmas was found to be roughly a factor of 2 larger than in deuterium (figure 15). However, the threshold in both H and D plasmas exhibits a strong dependence on the neutral beam torque [41], and the threshold in hydrogen plasmas with counter-injection was approximately the same as that of deuterium plasmas with strong co-injection. Beam emission spectroscopy (BES) measurements show that as neutral beam heating changes from co-injection to balanced injection, the turbulence velocity spectrum evolves to a low-frequency zonal flow which is more likely to suppress turbulence through shear flow, triggering the L–H transition [41]. Comparison of the H-mode phase of hydrogen and deuterium discharges with well-matched dimensionless parameters shows that the density fluctuation amplitude is about twice as large in the hydrogen plasmas, consistent with the lower energy confinement time observed.

5.3. H-mode pedestal

ITER's fusion performance will depend strongly on the characteristics of the H-mode edge transport barrier, and recent work has led to significant advances in the capability to predict the barrier height. Previous work [42] has shown that edge stability is consistent with limits set by peeling–ballooning modes with toroidal mode numbers $n \sim 3$–30. Recent experimental studies [43] using edge profile measurements with high spatial and temporal resolution, together with edge stability studies, motivate a simple empirical model of the pedestal width in normalized poloidal flux: $\Delta(\psi_N) = 0.076\beta_{p,ped}^{1/2}$. Combining this width model with direct calculations of MHD peeling–ballooning stability, which predict the pedestal height as a function of the width, yields a new predictive model (EPED1) for both the pedestal height and width [8]. An experiment was then designed to test this model, yielding very good agreement across an order of magnitude in pedestal height (figure 16(*a*)), in a data set that includes two 'ITER demonstration' cases where the shape, aspect ratio, safety factor and normalized beta were closely matched to those of the ITER baseline case (section 3.1). Comparison of the edge pressure profile in hydrogen and deuterium discharges with matched temperature, density and toroidal field (figure 16(*b*)) confirms the assumption that the pedestal width is insensitive to the ion gyroradius ρ_i^*, a favourable result for ITER. The EPED1 model yields a preliminary prediction of the pedestal temperature in ITER of 4.6 keV, which is in the range needed to achieve ITER's goal of $Q = 10$.

5.4. Quiescent H-mode

QH-mode plasmas in DIII-D have now been achieved with co-injected neutral beams [44, 45], where previously counter-injection was required. If it can be realized at ITER's operating parameters, the QH-mode represents a path to the desired conditions of a large edge pressure gradient but without the impulsive heat load generated by ELMs. The co-injected QH-mode has the expected features (figure 17(*a*)): ELM-free operation (for almost 1 s), constant density and constant radiated power, with a continuous MHD mode that limits the pressure gradient at the edge. This edge harmonic oscillation (EHO) is believed to be a saturated kink-peeling mode located near the edge of the plasma. A key element of these discharges is low-density operation with divertor cryopumping, allowing rapid toroidal rotation. Although the co-injected QH-mode shows strong co-rotation across the entire profile, it has a strong rotational shear at the edge similar to that of the counter-injected case (figure 17(*b*)), suggesting that rotational shear plays a key role in both cases. The existence of QH-mode with strong rotational shear for both co- and counter-rotation was predicted by theory [8]. If the required strong rotational shear can be generated, the QH-mode could represent a possible approach to ELM-free operation in ITER.

5.5. Transport physics

Confident extrapolation of fusion performance from present devices to ITER requires understanding of the transport physics, and there has been significant progress in this area. Improvement of diagnostic instruments combined with the addition of synthetic diagnostics to gyrokinetic transport calculations has allowed unprecedented comparison of theory and experiment [46–48]. Simultaneous, localized measurements of electron temperature fluctuations (with

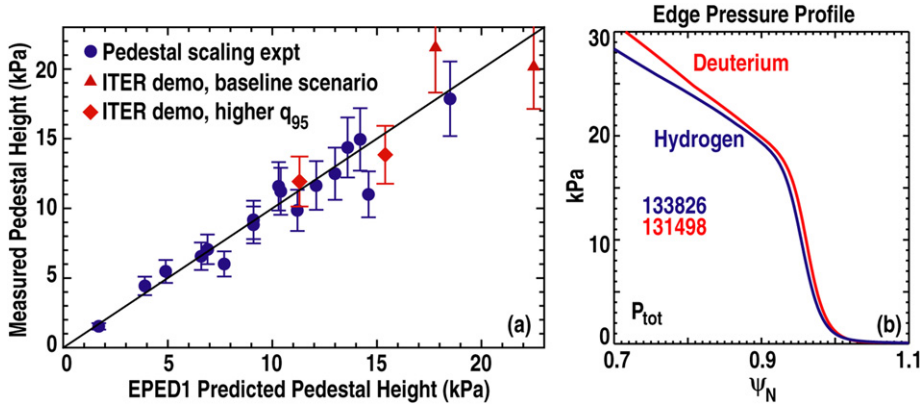

Figure 16. (*a*) Comparison of measured and predicted pedestal height for 21 DIII-D discharges with varying triangularity, plasma current and toroidal field. The prediction uses the EPED1 model. (*b*) Comparison of edge pressure profiles in hydrogen and deuterium plasmas.

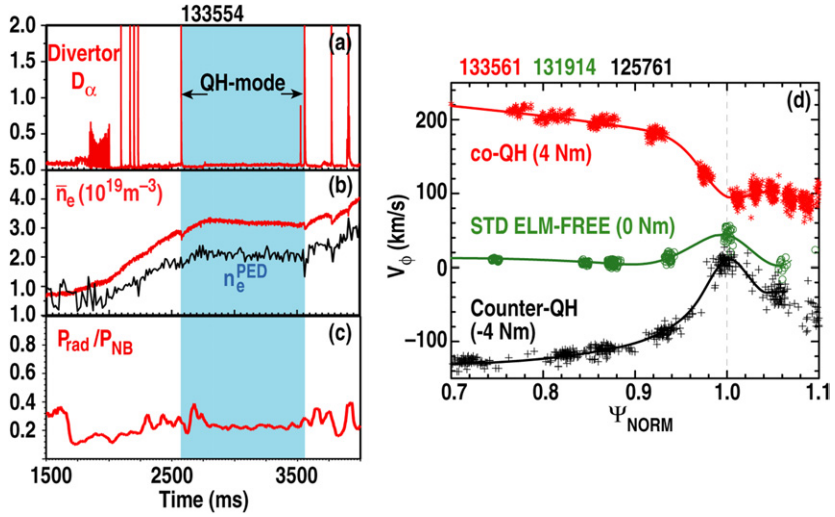

Figure 17. Time evolution of a QH-mode discharge with strong co-injection, showing (*a*) divertor D_α emission, (*b*) line-averaged density and pedestal density and (*c*) radiated power fraction. Also shown are (*d*) edge toroidal rotation profiles for cases with co (red), counter (black) and balanced (green) NBI. The co and counter cases are QH-mode and the balanced case is standard ELM-free H-mode.

Table 1. Comparison of measured and predicted heat flux at $r/a = 0.5$.

	Q_i (MW)	Q_e (MW)
Experiment	0.93 ± 0.16	0.74 ± 0.20
GYRO	1.1 ± 0.17	0.97 ± 0.14

correlation ECE) and density fluctuations (with BES) have been compared with GYRO code calculations, where the recent addition of synthetic diagnostics allows a quantitative comparison with experimental measurements. The measured and calculated density fluctuations show excellent agreement in spectral shape and amplitude (figure 18); the electron temperature comparison is hindered by a poorer signal to noise ratio but is in reasonable agreement. The ion and electron heat flux predicted by GYRO also show very good agreement with the experimentally measured values (table 1).

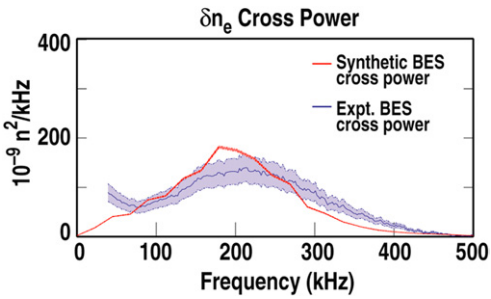

Figure 18. Comparison of density fluctuation spectrum at $r/a = 0.5$, as measured by BES and predicted by the GYRO code including synthetic diagnostic calculation.

5.6. Fast ions

New measurements in DIII-D are illuminating the physics of fast ion-driven instabilities and the associated fast-ion transport [49]; scientific understanding and well-benchmarked transport and stability models are needed to predict the behaviour of fusion alpha particles in ITER. Neutral beam injection into the current ramp phase of reversed magnetic shear DIII-D plasmas [50] typically excites a variety of Alfvénic activity including toroidicity and ellipticity induced Alfvén eigenmodes (TAEs and EAEs) and reversed shear Alfvén eigenmodes (RSAEs),

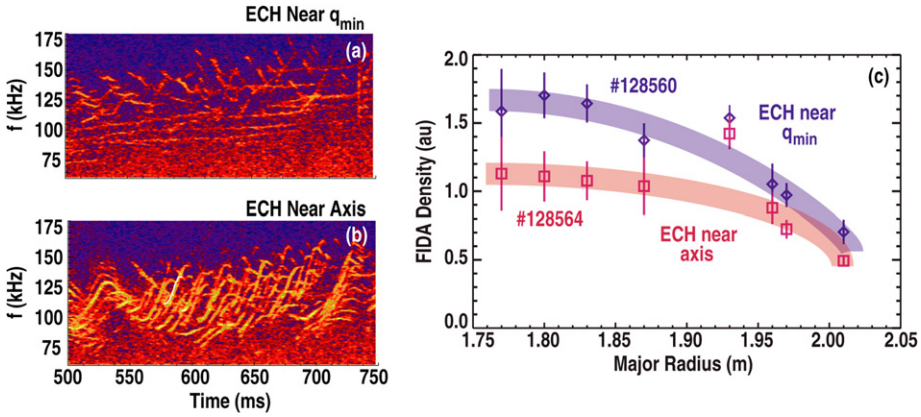

Figure 19. Cross power spectra of vertical and radial interferometer chords in the frequency range of Alfvén instabilities (*a*) during ECH deposition near the magnetic axis and (*b*) during ECH deposition near $q_{\min}$. Also shown are (*c*) profiles of fast-ion D_α (FIDA) measurements for the two cases in (*a*) and (*b*).

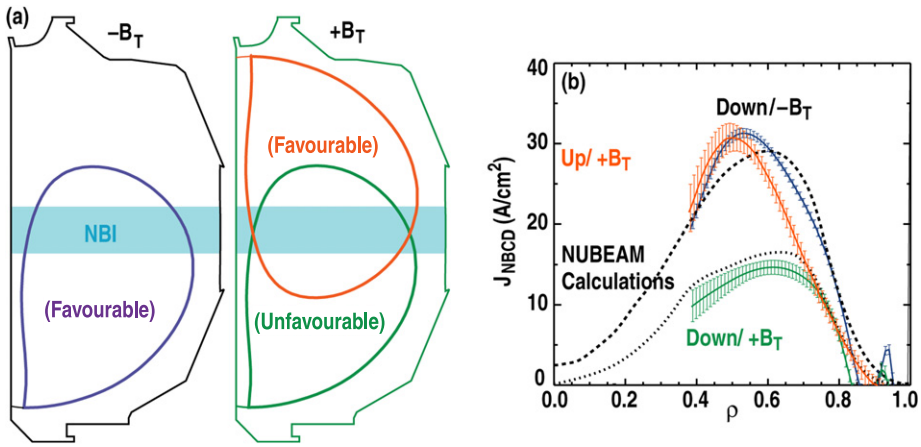

Figure 20. (*a*) Small, vertically shifted plasmas allow tests of off-axis beam injection, using upward and downward shifts and toroidal field in both directions. (*b*) Comparison of the experimentally measured neutral beam current drive (vertical bars) with transport model predictions (dotted curves). Both figures include two cases with favourable magnetic field pitch (orange and blue) and one case with unfavourable pitch (green).

which are revealed by fast interferometry (figures 19(*a*) and (*b*)) and fluctuation diagnostics such as ECE and BES. Fast-ion D_α (FIDA) spectroscopy [51] shows that the central fast ion profile is flattened and the degree of flattening depends on Alfvén eigenmode amplitude. However, ion orbit calculations based on linear eigenfunctions from the NOVA code [52] with measured mode amplitudes do not explain the observed fast-ion transport [53]; multimode simulations with time-varying mode frequencies may be needed. Recent experiments have found that localized ECH applied near the magnetic shear reversal location can stabilize RSAE activity (figures 19(*a*) and (*b*)), resulting in significantly improved fast ion confinement (figure 19(*c*)). FIDA measurements have also been used to measure fast wave absorption by energetic ions [54]. The recent capability for 2D imaging of fast-ion D_α emission with a fast framing camera provides a potentially powerful new tool for study of fast ion transport.

5.7. Off-axis neutral beam current drive

Non-inductive current driven by neutral beam injection will be off axis in ITER, by virtue of the vertical displacement of the injectors relative to the magnetic axis and also the capability for vertical steering. Off-axis neutral beam current drive may also provide an important means of sustaining the hollow current density profiles necessary for advanced scenarios in DIII-D and ITER. Recent experiments have validated models of off-axis current drive [55], using DIII-D's existing midplane injectors coupled to small, vertically shifted plasmas. As shown in figure 20, the agreement of the model with experiments results is very good. The figure also shows that the current drive efficiency is sensitive to the beam's alignment with the local magnetic field pitch. The strong dependence on alignment to the magnetic field may help to explain the lack of current drive localization reported in other off-axis NBI experiments [56]. The current drive was reduced by about 40% in the DIII-D case with unfavourable pitch; in ITER the difference could be about 20%.

6. Summary and future research directions

Recent DIII-D research has contributed to a wide range of topics in the design and physics basis of ITER. DIII-D experiments have helped to establish physics criteria for several

recent ITER design choices, including proposed new coils for ELM suppression and vertical stability. The performance capabilities for several ITER operating scenarios have been validated, and parameters equivalent to $Q = 10$ have been demonstrated in inductive and hybrid scenarios. Control solutions have been developed for several key issues of MHD stability and plasma interaction with surrounding materials, including high beta operation at near zero rotation, gas delivery systems for disruption mitigation and the effect of scrape-off-layer drifts on particle control. A broad range of fusion science studies provide the basis for prediction and improvement of ITER's performance, including plasma rotation, L–H transition, H-mode pedestal height, ELM-free QH mode operation, validation of turbulent transport codes, fast ion transport and off-axis neutral beam current drive.

Future DIII-D research will continue to address scientific and technical issues for ITER. New hardware capabilities are anticipated in the next several years to enable this research, including additional electron cyclotron power for profile control and non-inductive operation, extension of the heating systems' pulse lengths, high-density impurity delivery systems for disruption mitigation and operation with heated walls and divertor targets for reduction of hydrogenic species co-deposition. A new set of RMP coils will enable further study of the physics of the stochastic edge and ELM control. The planned modification of a neutral beam line for injection with variable vertical angle will allow studies of off-axis neutral beam current drive, as anticipated in ITER's steady-state scenarios. Detailed transport modelling [57] predicts that, in full-sized DIII-D plasmas, a vertically tilted beam line will provide up to 200 kA of current drive centred at mid-radius. Such experiments will support the use of off-axis NBI in ITER's steady-state scenarios. With these upgrades, DIII-D will continue to advance the physics basis for ITER until and beyond the time that ITER begins operation.

Appendix A: DIII-D Team

S.S. Abdullaev[1], G. Abla[2], T. Abrams[3], M.P. Aldan[4], N.B. Alexander[2], S.L. Allen[5], D. Anastasi[2], P.M. Anderson[2], M.E. Austin[6], F.W. Baity[7], J.P. Bakalarski[2], T. Barber[7], V. Basiuk[8], E.M. Bass[9], G. Bateman[10], C.B. Baxi[2], L.R. Baylor[7], M. Becoulet[8], E.A. Belli[9], H.L. Berk[6], J.W. Berkery[11], L.A. Berry[7], M. Beurskens[12], J.M. Bialek [11], J.A. Boedo[13], I.N. Bogatu[14], R.L. Boivin [2], A.H. Boozer[11], R.V. Bravenec[6], B.D. Bray[2], D.P. Brennan[15], S. Brezinsek[1], N.H. Brooks[2], L.C. Brown[2], C.D. Brunkhorst[16], R.V. Budny[16], R. Bulmer[5], K.H. Burrell[2], R.J. Buttery[12], J.D. Callen[17], R.W. Callis[2], G.L. Campbell[2], J.M. Candy[2], J. Canik[7], T.N. Carlstrom[2], T.A. Carter[18], R. Carver[19], W.P. Cary[2], A. Casati[8], T.A. Casper[5], A. Castano[16], M. Cengher[2], C.D. Challis[12], F.R. Chamberlain[2], V.S. Chan[2], M.S. Chance[16], S. Chang[20], S.N. Chen[3], R. Chipman[21], H.K. Chiu[2], M. Choi[2], M.S. Chu[2], R.J. Colchin[7], A.J. Cole[17], G. Colyer[12], S.K. Combs[7], N. Commaux[7], W.A. Cooper[22], D. Coster[23], J. Dalessio[10], J.W. Davis[24], J.C. DeBoo[2], J.S. deGrassie[2], S.J. DePasquale[16], T.M. Deterly[2], J.L. Doane[2], M. Dorris[3], E.J. Doyle[18], N. Eidietis[9], D. Elder[24], R. Ellis[5], R.A. Ellis[16], R.F. Ellis[25], T.E. Evans[2], M. Fahey[7], R. Feder[16], D. Fehling[7], E.A. Feibush[16], Y. Feng[26], M.E. Fenstermacher[5], M. Ferrara[3], J.R. Ferron[2], K.H. Finken[1], D.K. Finkenthal[27], R.K. Fisher[2], D. Fitzpatrick[24], B.W.N. Flanagan[2], S.M. Flanagan[15], R.J. Fonck[17], J.M. Foster[28], E. Fredd[16], R. Freeman[29], H.G. Frerichs[1], R.K. Friend[30], Z. Friis[31], G.Y. Fu[16], Q. Gao[32], A.M. Garofalo[2], K.W. Gentle[6], A. Geraud[8], P. Gohil[2], N.N. Gorelenkov[16], I.A. Gorelov[2], P.A. Gourdain[18], K.L. Greene[2], C.M. Greenfield [2], N.L. Greenough[16], R.J. Groebner[2], M. Groth[5], H.J. Grunloh[2], M.F. Gu[5], W. Guo[33], A.A. Haasz[24], S.H. Hahn[34], F.D. Halpern[10], J. Hansink[2], J. Harhausen[23], J.H. Harris[35], P. Hartigan[19], D. Harting[1], R.W. Harvey[36], N.C. Hawkes[12], R.J. Hawryluk[16], C. Hegna[17], W.W. Heidbrink[37], M.F. Heyn[38], D.N. Hill[5], D.L. Hillis[7], J. Hillscheim[18], J.K. Hobirk[39], C.T. Holcomb[5], C. Holland[13], E.M. Hollmann[13], K.L. Holtrop[2], R.M. Hong[2], L. Horton[23], J.C. Hosea[16], C.L. Hsieh [2], A.E. Hubbard[3], A. Huber[1], B. Hudson[9], J. Hughes[3], D.A. Humphreys[2], I.H. Hutchinson[3], P. Huynh[2], G.T.A. Huysmans[8], A.W. Hyatt[2], S. Ide[40], F. Imbeaux[8], Y. In[14], K. Indireshkumar[16], A. Isayama[40], R.C. Isler[7], I.B. Ivanov[38], V.A. Izzo[13], G.L. Jackson[2], A.M. Jacobs[41], E.F. Jaeger[7], M. Jakubowski[1], A.N. James[13], R.J. Jayakumar[5], Y.M. Jeon[9], T.C. Jernigan[7], E.H. Joffrin[8], P. Johnson[42], R.D. Johnson[2], I. Joseph[5], K. Kajiwara[9], A. Kallenbach[23], Y. Kamada[40], D.H. Kaplan[2], S.V. Kasilov[38], A. Kasugai[40], K.M. Keith[2], A.G. Kellman[2], D.H. Kellman[2], J. Kim[14], J.S. Kim[14], J.E. Kinsey[2], C. Konz[26], M. Kotschenreuther[6], G.J. Kramer[16], S.I. Krasheninnikov[13], A.H. Kritz[10], R.J. La Haye[2], B. Labombard[3], M.J. Lanctot[11], L.L. Lao[2], C.J. Lasnier[5], E.A. Lazarus[7], R.L. Lee[2], X. Lee[2], M. Lehnen[1], A.W. Leonard[2], J.A. Leuer[2], F.M. Levinton[43], J. Li[33], L. Li[33], B. Lipschultz[3], J. Lister[22], Y.Q. Litnovsky[1], A. Liu[2], D. Liu[37], C. Liu[12], L.L. Lodestro[5], N. Logan[44], J. Lohr[2], T.C. Luce[2], C.A. Ludescher-Furth[16], Y. Luo[37], C.F. Maggi[23], S.M. Mahajan[1], S.B. Mahar[17], M.A. Mahdavi[45], J. Maillou [12], R. Maingi[7], M.A. Makowski[5], M.E. Maraschek[23], M. Marrelli[46], L. Martin[46], P. Martin[47], P.S. Mauzey[2], D. Mazon[8], S. McClain[21], D.C. McCune[16], W.L. McDaniel[2], B.B. McHarg[2], G.R. McKee[17], A.G. McLean[24], A. Meyer[5], D. Mikkelsen[16], D.C. Miller[2], D.W. Miller[16], C.P. Moeller[2], P. Monier-Garbet[8], S. Mordijck[13], K. Morris[5], R.A. Moyer[13], Y.R. Mu[24], S. Müller[13], M. Murakami[7], C.J. Murphy[2], C. Muscatello[37], A. Nagy[16], E. Nardon[8], M.F.A. Nave[48], G.A. Navratil[11], R. Nazikian[16], X.V. Nguyen[18], A. Nikroo[2], S. Noraky[2], R.E. Nygren[49], R.C. O'Neill[2], Y. Oda[40], Y.K. Oh[50], M. Okabayashi[16], R.A. Olstad[2], D. Orlov[13], T.H. Osborne[2], Y. Ou[10], L.W. Owens[7], N Oyama[40], N.A. Pablant[13], J. Palmer[19], C. Pan [33], A.Y. Pankin[10], J.K. Park[20], G. Park[7], J.M. Park[16], C.T. Parker[2], P.B. Parks[2], C.J. Pawley[2], L.D. Pearlstein[5], W.A. Peebles[18], B. Pegourie[8], B.G. Penaflor[2], P.I. Petersen[2], T.W. Petrie[2], C.C. Petty[2], N.Q. Pham[2], V. Philipps[1], A.Yu. Pigarov[13], D.A. Piglowski[2], R.I. Pinsker[2], P.A. Politzer[2], D.M. Ponce[2], M. Porkolab[3], G.D. Porter[5], A. Pospieszezyk[1], R. Prater[2], J. Qian[33], T. Rafiq[10], D. Raju[51], M. Ramm[52], L.E. Randerson[16], H. Reimerdes[11], D. Reiser[1], Q. Ren[33], M.E. Rensink[5], G. Rewoldt[16], T.L. Rhodes[18], H. Rinderkhecht[16], T.D. Rognlien[5], P.A. Rosen[28], M. Rosenberg[13], J.C. Rost[3], R. Rubilar[17], D.L. Rudakov[13], A. Runov[26], E. Ruskov[37], P.M. Ryan[7], D. Ryutov[5], S. Saarelma[12], S.A. Sabbagh[11], G. Saibene[23], Y. Sakamoto[40], U. Samm[1], B.S. Sammuli[2], F. Sartori[12], R.I. Savercool[2],

M.J. Schaffer[2], D.P. Schissel[2], D.J. Schlossberg[17], O. Schmitz[1], L. Schmitz[18], D.G. Schneider[8], E. Schuster[10], J.T. Scoville[2], S. Sears[53], A. Sen[51], M.W. Shafer[17], J.P. Sharpe[54], T.Y. Sheffield[55], J.Y. Shiriashi[9], K.C. Shoolbred[2], R.D. Sips[23], A.C.C. Smirnov[56], A.P. Smirnov[13], J.P. Smith[2], P.B. Snyder[2], W.M. Solomon[16], R. Srinivason[51], H.E. St. John[2], W.M. Stacey[31], G.M. Staebler[2], R.D. Stambaugh[2], P.C. Stangeby[24], C. Stemprok[2], N.C. Stone[47], E.J. Strait[2], R.W. Street[2], J.D. Stromsoe[13], T. Suzuki[40], W.S. Sweet[2], H. Takahashi[16], D.A. Taussig[2], P.L. Taylor[2], T.S. Taylor[2], W. Terry[3], D.M. Thomas[2], M. Tillack[13], M. Tokar[1], J.F. Tooker[2], Y. Treutterer[23], J. Tucci[57], F. Turco[9], A.D. Turnbull[2], G.R. Tynan[13], M. Umansky[5], K. Umstadter[13], E.A. Unglaub[58], W. Unterberg [1], B. Unterberg[9], H. Urano[40], P. Valanju[6], E. Valeo[16], M.A. VanZeeland[2], S. Visser[2], G. Vlad[59], F. Volpe[23], J. Von Der Lindon[60], M.R. Wade[2], M.L. Walker[2], R.E. Waltz[2], W.R. Wampler[49], B. Wan[33], S.J. Wang[33], A. Wang[32], G. Wang[18], J.G. Watkins[49], A.S. Welander[2], J.C. Wesley[2], W.P. West[2], B. White[16], R. White[18], D.G. Whyte[3], R.J.R. Williams[28], H.R. Wilson[61], A. Wingen[62], M. Wischmeier[23], R. Wolf[26], S.M. Wolfe[3], C.P.C. Wong[2], N. Wong[2], S.K. Wong[5], W. Wu[2], B. Xiao[33], H.W. Xu[2], X. Xu [5], S. Yang[10], H.H. Yip[2], Y.S. Yoon[63], D. Young [64], J.H. Yu[13], Q. Yuan[33], H. Yuh[43], L. Zeng [18] and Y. Zhu[37].

Affiliations

[1] EURATOM-FZ Julich, Germany
[2] General Atomics, USA
[3] Massachusetts Institute of Technology, USA
[4] University of California, Berkeley, USA
[5] Lawrence Livermore National Laboratory, USA
[6] University of Texas, USA
[7] Oak Ridge National Laboratory, USA
[8] CEA Cadarache Euratom Association, France
[9] LeHigh University, USA
[10] Oak Ridge Institute of Science Education, USA
[11] Columbia University, USA
[12] UKAEA Fusion Culham Science Centre, UK
[13] University of California, San Diego, USA
[14] FARTECH, Inc., USA
[15] University of Tulsa, USA
[16] Princeton Plasma Physics Laboratory, USA
[17] University of Wisconsin, USA
[18] University of California, Los Angeles, USA
[19] Rice University, USA
[20] New York University, USA
[21] University of Arizona, USA
[22] CRPP-EPFL-Lausanne, Switzerland
[23] Max-Planck-Institut für Plasmaphysik, Garching, Germany
[24] University of Toronto, Canada
[25] University of Maryland, USA
[26] Max-Planck–Greifswald, Germany
[27] Palomar College, USA
[28] AWE Communications, Germany
[29] Ohio State University, USA
[30] Washington & Lee University, USA
[31] Georgia Institute of Technology, USA
[32] SWIPP, Chengdu, China
[33] ASIPP-Hefei, China
[34] National Fusion Research Center, Korea
[35] Australian National University, Australia
[36] CompX, USA
[37] University of California, Irvine, USA
[38] Euratom-ÖAW ITP Graz, Austria
[39] Max Planck Institute, Germany
[40] Japan Atomic Energy Agency (JAEA), Japan
[41] Hendrix College, USA
[42] Butler University, USA
[43] Nova Photonics, USA
[44] Brown University, USA
[45] ALITRON
[46] Consorzio RFX, Italy
[47] Cornell University, USA
[48] EURATOM Lisbon, Portugal
[49] Sandia National Laboratory, USA
[50] National Fusion Research Institute, Korea
[51] Institute for Plasma Research, India
[52] Stanford University, USA
[53] West Virginia University, USA
[54] Idaho National Laboratory, USA
[55] TCU, USA
[56] Moscow State University, Russia
[57] Notre Dame University, USA
[58] Colorado School of Mines, USA
[59] ENEA-Frascati, Italy
[60] University of Pennsylvania, USA
[61] University of York, UK
[62] University of Düsseldorf, Germany
[63] Korea Atomic Energy Research Institute, Korea
[64] National Renewable Energy Laboratory, USA

Acknowledgment

This work was supported by the US Department of Energy under DE-FC02-04ER54698.

References

[1] Hawryluk R.J. for the ITER organization, ITER domestic agencies and ITER collaborators 2009 *Nucl. Fusion* **49** 065012
[2] Thomas P.R. for the ITER organization, ITER domestic agencies and ITER collaborators 2008 *Proc. 22nd Int. Conf. on Fusion Energy 2008 (Geneva, Switzerland, 2008)* (Vienna: IAEA) paper IT/1-5 http://www-naweb.iaea.org/napc/physics/FEC/FEC2008/html/index.htm
[3] Portone A *et al* 2008 *Proc. 22nd Int. Conf. on Fusion Energy 2008 (Geneva, Switzerland, 2008)* (Vienna: IAEA) paper IT/2-4Ra http://www-naweb.iaea.org/napc/physics/FEC/FEC2008/html/index.htm
[4] Loarte A. *et al* 2008 *Proc. 22nd Int. Conf. on Fusion Energy 2008 (Geneva, Switzerland, 2008)* (Vienna: IAEA) paper IT/P6-13 http://www-naweb.iaea.org/napc/physics/FEC/FEC2008/html/index.htm
[5] Evans T.E. *et al* 2008 *Proc. 22nd Int. Conf. on Fusion Energy 2008 (Geneva, Switzerland, 2008)* (Vienna: IAEA) paper EX/4-1 http://www-naweb.iaea.org/napc/physics/FEC/FEC2008/html/index.htm
[6] Fenstermacher M.E. *et al* 2008 *Phys. Plasmas* **15** 056122

[7] Fenstermacher M.E, Evans T.E., Osborne T.H., Schaffer M.J., deGrassie J.S., Gohil P., Moyer R.A. and the DIII-D Team 2008 *Nucl. Fusion* **48** 122001
[8] Snyder P.B. *et al* 2009 *Nucl. Fusion* **49** 085035
[9] Izzo V.A., Joseph I., Moyer R.A., Evans T.E., Fenstermacher M.E., Osborne T.H., Lao L.L. and Snyder P.B. 2008 *Proc. 22nd Int. Conf. on Fusion Energy 2008 (Geneva, Switzerland, 2008)* (Vienna: IAEA) paper TH/P4-19 http://www-naweb.iaea.org/napc/physics/FEC/FEC2008/html/index.htm
[10] Baylor L.R. *et al* 2009 *Nucl. Fusion* **49** 085013
[11] Humphreys D.A. *et al* 2009 Experimental vertical stability studies for ITER performance and design guidance *Nucl. Fusion* **49** at press
[12] Doyle E.J. *et al* 2008 *Proc. 22nd Int. Conf. on Fusion Energy 2008 (Geneva, Switzerland, 2008)* (Vienna: IAEA) paper EX/1-3 http://www-naweb.iaea.org/napc/physics/FEC/FEC2008/html/index.htm
[13] Yushmanov P.N., Takizuka T., Riedel K.S., Kardaun J.W.-F., Cordey J.G., Kaye S.M. and Post D.E. 1990 *Nucl. Fusion* **30** 1999
[14] Petty C.C. *et al* 2008 *Proc. 22nd Int. Conf. on Fusion Energy 2008 (Geneva, Switzerland, 2008)* (Vienna: IAEA) paper EX/1-4Rb http://www-naweb.iaea.org/napc/physics/FEC/FEC2008/html/index.htm
[15] Jackson, G.L., Casper T.A., Luce T.C., Humphreys D.A., Ferron J.R., Hyatt A.W., Petrie T.W. and West W.P. 2009 Simulating ITER plasma startup and rampdown scenarios in the DIII-D tokamak *Nucl. Fusion* submitted
[16] Ferron J.R. *et al* 2008 *Proc. 22nd Int. Conf. on Fusion Energy 2008 (Geneva, Switzerland, 2008)* (Vienna: IAEA) paper EX/P4-27 http://www-naweb.iaea.org/napc/physics/FEC/FEC2008/html/index.htm
[17] Reimerdes H. *et al* 2009 Effect of resonant and non-resonant magnetic braking on error field tolerance in high beta plasmas *Nucl. Fusion* **49** at press
[18] Liu Y.Q., Bondeson A., Fransson C.M., Lennartson B. and Breitholz C. 2000 *Phys. Plasmas* **7** 3681
[19] Buttery R.J. *et al* 2008 *Proc. 22nd Int. Conf. on Fusion Energy 2008 (Geneva, Switzerland, 2008)* (Vienna: IAEA) paper IT/P6-8 http://www-naweb.iaea.org/napc/physics/FEC/FEC2008/html/index.htm
[20] Buttery R.J., La Haye R.J., Gohil P., Jackson G.L., Reimerdes H., Strait E.J. and the DIII-D Team 2008 *Phys. Plasmas* **15** 56115
[21] La Haye R.J., Isayama A., Maraschek M., for the DIII-D, JT-60 and ASDEX Upgrade Teams 2009 *Nucl. Fusion* **49** 045005
[22] Van Zeeland M.A., Yu J.H., Chu M.S., Burrell K.H., La Haye R.J., Luce T.C., Nazikian R., Solomon W.M. and West W.P. 2008 *Nucl. Fusion* **48** 092002
[23] Reimerdes H. *et al* 2007 *Plasma Phys. Control. Fusion* **49** B349
[24] Okabayashi M. *et al* 2009 Comprehensive control of resistive wall modes in DIII-D advanced tokamak plasmas *Nucl. Fusion* submitted
[25] Granetz R.S. *et al* 2007 *Nucl. Fusion* **47** 1086
[26] Hollmann E.M. *et al* 2008 *Nucl. Fusion* **48** 115007
[27] Izzo V.A., Whyte D.G., Granetz R.S., Parks P.B., Hollmann E.M., Lao L.L. and Wesley J.C. 2008 *Phys. Plasmas* **15** 056109
[28] Wesley J.C. *et al* 2008 *Proc. 22nd Int. Conf. on Fusion Energy 2008 (Geneva, Switzerland, 2008)* (Vienna: IAEA) paper EX/7-3Rb http://www-naweb.iaea.org/napc/physics/FEC/FEC2008/html/index.htm
[29] Petrie T.W. *et al* 2008 *Nucl. Fusion* **48** 045010
[30] Petrie T.W. *et al* 2009 *Nucl. Fusion* **49** 065013
[31] Rognlien T., Milovich J.L., Rensink M.E. and Porter G.D. 1992 *J. Nucl. Mater.* **196–198** 347
[32] Groth M. *et al* 2009 Effect of cross-field drifts on flows in the main scrape-off layer of DIII-D L mode plasmas *Nucl. Fusion* **49** at press
[33] Rudakov D.L. *et al* 2009 *Nucl. Fusion* **49** 085022
[34] Litnovsky A. *et al* 2008 *Fusion Eng. Des.* **83** 79
[35] Davis J.W. and Haasz A.A. 2009 *J. Nucl. Mater.* **390–391** 532
[36] Solomon W.M. *et al* 2009 *Nucl. Fusion* **49** 085005
[37] deGrassie J.S., Groebner R.J., Burrell K.H. and Solomon W.M. 2009 *Nucl. Fusion* **49** 085020
[38] Garofalo A.M., Burrell K.H., DeBoo J.C., deGrassie J.S., Jackson G.L., Lanctot M.J., Reimerdes H., Schaffer M.J., Solomon W.M. and Strait E.J. 2008 *Phys. Rev. Lett.* **101** 195005
[39] Gohil P., McKee G.R., Schlossberg D.J., Schmitz L. and Wang G. 2008 *J. Phys.: Conf. Ser.* **123** 12017
[40] Gohil P. *et al* 2009 The H-mode power threshold in hydrogen plasmas in DIII-D *Nucl. Fusion* **49** at press
[41] McKee G.R. *et al* 2009 Dependence of the L- to H-mode power threshold on toroidal rotation and the link to edge turbulence dynamics *Nucl. Fusion* **49** at press
[42] Snyder P.B. *et al* 2007 *Nucl. Fusion* **47** 961
[43] Groebner R.J., Leonard A.W., Snyder P.B., Osborne T.H., Maggi C.F., Fenstermacher M.E., Petty C.C. and Owen L.W. 2009 *Nucl. Fusion* **49** 085037
[44] Burrell K.H., Osborne T.H., Snyder P.B., West W.P., Fenstermacher M.E., Groebner R.J., Gohil P., Leonard A.W. and Solomon W.M. 2009 *Nucl. Fusion* **49** 085024
[45] Burrell K.H., Osborne T.H., Snyder P.B., West W.P., Fenstermacher M.E., Groebner R.J., Gohil P., Leonard A.W. and Solomon W.M. 2009 *Phys. Rev. Lett.* **102** 155003
[46] White A.E. *et al* 2008 *Phys. Plasmas* **15** 056116
[47] Schmitz L. *et al* 2009 *Nucl. Fusion* **49** 095004
[48] Holland C., Waltz R.E., Candy J., McKee G.R., Shafer M.W., White A.E., Schmitz L. and Tynan G.R. 2008 *Proc. 22nd Int. Conf. on Fusion Energy 2008 (Geneva, Switzerland, 2008)* (Vienna: IAEA) paper TH/8-1 http://www-naweb.iaea.org/napc/physics/FEC/FEC2008/html/index.htm
[49] Van Zeeland M.A. *et al* 2009 *Nucl. Fusion* **49** 065003
[50] Nazikian R. *et al* 2008 *Phys. Plasmas* **15** 056107
[51] Heidbrink W.W., Luo Y., Muscatello C.M., Zhu Y. and Burrell K.H. 2008 *Rev. Sci. Instrum.* **79** 10E520
[52] Cheng C.Z. 1992 *Phys. Rep.* **1** 211
[53] Heidbrink W.W. *et al* 2007 *Phys. Rev. Lett.* **99** 245002
[54] Pinsker R.I. *et al* 2008 *Proc. 22nd Int. Conf. on Fusion Energy 2008 (Geneva, Switzerland, 2008)* (Vienna: IAEA) paper EX/P6-24 http://www-naweb.iaea.org/napc/physics/FEC/FEC2008/html/index.htm
[55] Murakami M. *et al* 2009 *Nucl. Fusion* **49** 065031
[56] Günter S. *et al* 2007 *Nucl. Fusion* **47** 920
[57] Murakami M., Park J.M., Luce T.C., Wade M.R., Hong R.M. 2008 *Fusion Sci. Techol.* **54** 994